Strong pinning and vortex energy distributions in single-crystalline Ba(Fe$_{1-x}$Co$_x$)$_2$As$_2$

S. Demirdiş and C. J. van der Beek

Laboratoire des Solides Irradiés, CNRS UMR 7642 & CEA-DSM-IRAMIS, Ecole Polytechnique, F-91128 Palaiseau cedex, France

Y. Fasano, N. R. Cejas Bolecek, and H. Pastoriza

Laboratorio de Bajas Temperaturas, Centro Atómico Bariloche & Instituto Balseiro, Avenida Bustillo 9500, 8400 Bariloche, Argentina

D. Colson and F. Rullier-Albenque

Service de Physique de l' Etat Condensé, L' Orme des Mérisiers, CEA-DSM-IRAMIS, F-91198 Gif-sur-Yvette, France

The interrelation between heterogeneity and flux pinning is studied in Ba(Fe$_{1-x}$Co$_x$)$_2$As$_2$ single crystals with widely varying Co content x. Magnetic Bitter decoration of the superconducting vortex ensemble in crystals with $x = 0.075$ and $x = 0.1$ reveals highly disordered vortex structures. The width of the Meissner belt observed at the edges of the crystals, and above the surface steps formed by cleaving, as well as the width of the intervortex distance distribution, indicate that the observed vortex ensemble is established at a temperature just below the critical temperature T_c. The vortex interaction energy and pinning force distributions extracted from the images strongly suggest that the vortex lattice disorder is attributable to strong pinning due to spatial fluctuations of T_c and of the superfluid density. Correlating the results with the critical current density yields a typical length scale of the relevant disorder of 40–60 nm.

PACS number(s): 74.25.Wx, 74.25.Sv, 74.62.En, 74.70.Xa

I. INTRODUCTION

Recent vortex imaging studies of iron-based superconductors have unveiled highly disordered vortex structures that challenge the use of traditional analysis procedures based on the characterization of positional and orientational lattice correlations.[1–7] For example, the combination of small-angle neutron scattering experiments with Bitter decoration[1,2] and magnetic force microscopy[3] revealed a "vitreous" phase in Ba(Fe$_{1-x}$Co$_x$)$_2$As$_2$ single crystals. The latter work shows that the vortex structure of the overdoped material ($x = 0.19$) presents, at best, short-range hexagonal order in the field range of 10^{-3} to 9 T. Disordered vortex structures were also observed by means of Bitter decoration in single crystals of other iron-based pnictide superconductors including Ba$_{1-x}$K$_x$Fe$_2$As$_2$, Sr$_{1-x}$K$_x$Fe$_2$As$_2$, and SmAsO$_{1-x}$F$_x$.[4] Regardless of material, doping, and synthesis method, the disordered vortex structures are attributed to a strong pinning the nature of which was not discussed.

The only reported ordering effect on the orientation of the vortex ensemble is that induced by twin boundaries in Ba(Fe$_{0.949}$Co$_{0.051}$)$_2$As$_2$.[5] This scanning superconducting quantum interference device (scanning SQUID) microscopy study shows that vortices avoid twin boundaries acting as a barrier for vortex motion.[5] These results echo earlier work on the doping dependence of the critical current density j_c, which suggests that structural domain walls may act as effective pinning centers in the underdoped material.[8]

Concerning the nature of the strong pinning ubiquitous to iron-based superconductors, inhomogeneities in the dopant-ion distribution was suggested to be at the origin of a dense vortex pinning nanostructure in the case of Ba(Fe$_{1-x}$Co$_x$)$_2$As$_2$ ($x = 0.1$).[9] The same study shows that since thermal fluctuations are weak, the finite width of the superconducting transition can only be ascribed to an inhomogeneous T_c

distribution due to local compositional variations.[9] Furthermore, scanning tunneling spectroscopy studies in different iron-based pnictides reveal nanoscale variations of the local superconducting gap.[10–12] In Ba(Fe$_{1-x}$Co$_x$)$_2$As$_2$, the length scale on which the deviations from the average gap value occur is comparable to the average distance between dopant ions.[11] Nevertheless, no correlation between the vortex positions and the superconducting-gap inhomogeneities or other defects has, as yet, been found.[7]

Hence, all techniques agree on the absence of an ordered vortex structure in iron-based superconductors. However, there is no clear consensus on the origin of the disorder in the vortex ensemble and the pinning causing it. The aim of this paper is the characterization of this strong pinning by means of a quantitative analysis of the spatial distributions of pinning energy and pinning force. We found that the key to understand the disordered vortex configurations is that these are frozen at $T \sim T_c$, in crystals with important spatial variations of the superconducting parameters. The correlation of the extracted pinning forces and energies with measurements of j_c indicates that spatial variations of the superfluid density and of T_c, on the scale of several to several dozen nm, are the most relevant for pinning.

II. EXPERIMENTAL DETAILS

Single crystals of Ba(Fe$_{1-x}$Co$_x$)$_2$As$_2$ were grown using the self-flux method.[13] Starting reagents of high-purity Ba, FeAs, and CoAs were mixed in the molar ratio 1 : $(4 - x)$: x, loaded in alumina crucibles, and then sealed in evacuated quartz tubes. For each doping level, chemical analysis by an electron probe was performed on several crystals yielding the Co content within 0.5% absolute accuracy. For this work we studied six doping levels.

The penetration of magnetic flux into selected crystals of thickness 30 μm was visualized by the magneto-optical imaging (MOI) method.[15] A ferrimagnetic garnet indicator film with in-plane anisotropy is placed on top of the sample and a polarized light microscope is used to observe it. The Faraday rotation of the indicator allows the detection of regions with nonzero perpendicular component of the magnetic flux density $B_\perp$, revealed as bright when observed through an analyzing polarizer. Dark regions correspond to $B_\perp \approx 0$. In order to characterize the inhomogeneity of the crystals in the vicinity of the critical temperature we use the differential magneto-optical method (DMO).[16] Images acquired at applied fields $H_a + \Delta H_a$ and H_a are subtracted, and the differential images averaged by repeating the procedure 50 times. In the present experiments $\mu_0 \Delta H_a = 0.1$ mT (with $\mu_0 \equiv 4\pi \times 10^{-7}$ H m^{-1}).

The field dependence of the global critical current density of selected crystals was obtained from magnetization-loop measurements conducted using a Quantum Design SQUID magnetometer. The critical current densities were extracted using the Bean critical state model. As discussed below, the assumption of this model is justified by the way flux penetrates into the crystals. Within the Bean model, $j_c = 3\mathcal{M}/Va$, where $\mathcal{M}$ is the magnetic moment, V is the sample volume, and $2a$ is the sample width.[14]

For the Bitter decoration experiments,[17] rectangles of dimension 200×300 μm were cut from larger crystals using a 20 μm wire saw and 1 μm SiC grit. Bitter decorations were only performed on crystals with $x = 0.055$, $x = 0.075$, and $x = 0.1$. The sample surfaces were freshly cleaved before the experiments [Figs. 1(a) and 1(b)]. The experiments were carried out at liquid-helium temperature (4.2 K) and He-exchange gas at pressures of the order of 200 mTorr. The images shown here are the result of field-cooling experiments at a field $\mu_0 H_a = 1$ mT applied parallel to the c axis of the crystals. The decorated vortex arrangement was observed by scanning electron microscopy at room temperature.

III. RESULTS

A. Magneto-optical imaging and j_c measurements

Figure 1(c) shows examples of magneto-optical images, here obtained at $T = 15$ K on single crystal 2 of the composition with $x = 0.075$. The images reveal a globally homogeneous penetration of the magnetic flux into the sample obeying the Bean critical state.[18,19] We obtain the local value of the critical current density from $j_c \sim 6\partial B_\perp/\partial x$ (the factor 6 is estimated from Ref. 14 for a crystal aspect ratio of 0.1). The DMO images in Fig. 1(d) reveal the same Bean-like flux penetration with an inhomogeneous j_c arising from the spatial variation of T_c.

This inhomogeneity can be quantified using a plot of the local transmissivity, defined as the ratio $\mathcal{T}_H = [I(\mathbf{r},T) - I(\mathbf{r},T \ll T_c)]/[I(\mathbf{r},T \gg T_c) - I(\mathbf{r},T \ll T_c)]$ of the relative local luminous intensities $I(\mathbf{r},T)$ in the DMO images. The temperature dependence of $\mathcal{T}_H$ measured on different regions of crystals 2 and 1 is depicted in Figs. 1(e) and 1(f). The local variation of T_c values within a given crystal is of the order of 0.5–1 K. In addition, regions of lower T_c give rise to a
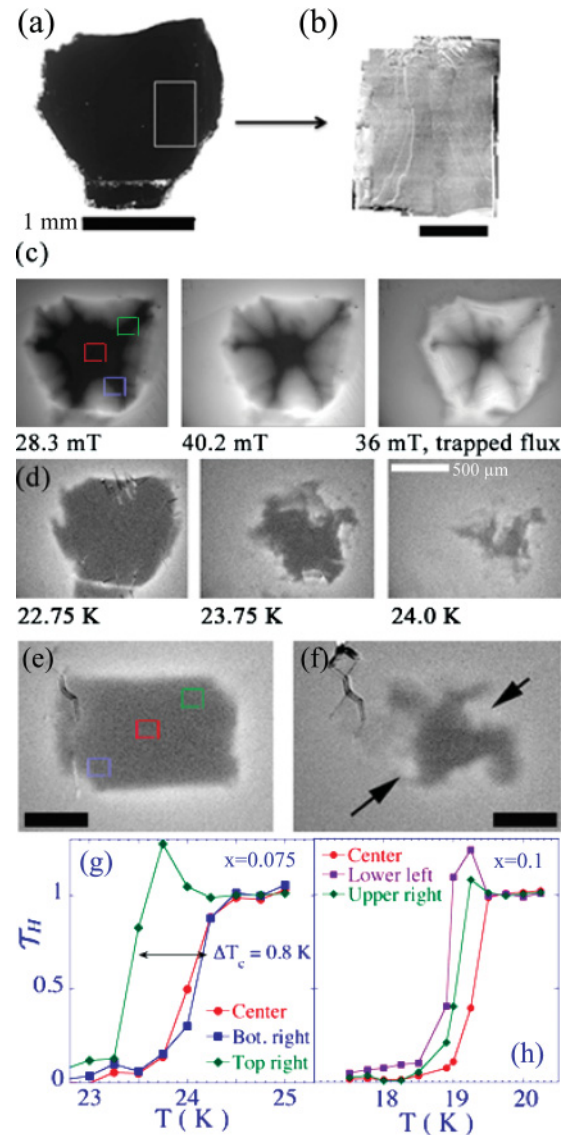

FIG. 1. (Color online) (a) Photograph of Ba(Fe$_{0.925}$Co$_{0.075}$)$_2$As$_2$ crystal 2. (b) Scanning electron micrograph of the decorated sample 2.1 cut from the larger crystal 2. (c) Magneto-optical images of Ba(Fe$_{0.925}$Co$_{0.075}$)$_2$As$_2$ crystal 2 at $T = 15$ K and indicated values of the applied magnetic field. (d) Differential magneto-optical (DMO) images in the vicinity of T_c for $\mu_0 \Delta H_a = 0.1$ mT. (e) DMO image of Ba(Fe$_{0.9}$Co$_{0.1}$)$_2$As$_2$ crystal 1 at full screening ($T = 17.5$ K) and (f) at midtransition ($T = 19.25$ K). The arrows indicate regions of paramagnetic transmissivity at the superconducting transition. (g) Local transmissivity $\mathcal{T}_H$ measured on the three regions of Ba(Fe$_{0.925}$Co$_{0.075}$)$_2$As$_2$ crystal 2. (h) $\mathcal{T}_H$ measured on the three regions of Ba(Fe$_{0.9}$Co$_{0.1}$)$_2$As$_2$ crystal 1 indicated in (e). Scale bars correspond to a length of 100 μm unless indicated otherwise.

paramagnetic signal at the transition due to flux concentration by the surrounding superconducting parts of the crystal.

Figure 2(a) summarizes the width of the T_c distribution for a large number of Ba(Fe$_{1-x}$Co$_x$)$_2$As$_2$ single crystals of different doping levels. Figure 2(b) shows the Co doping level dependence of j_c for the same series of single crystals at a reduced temperature of $T/T_c = 0.47$. A rather large sample-to-sample variation of the low-field ($B_\perp = 30$ mT)
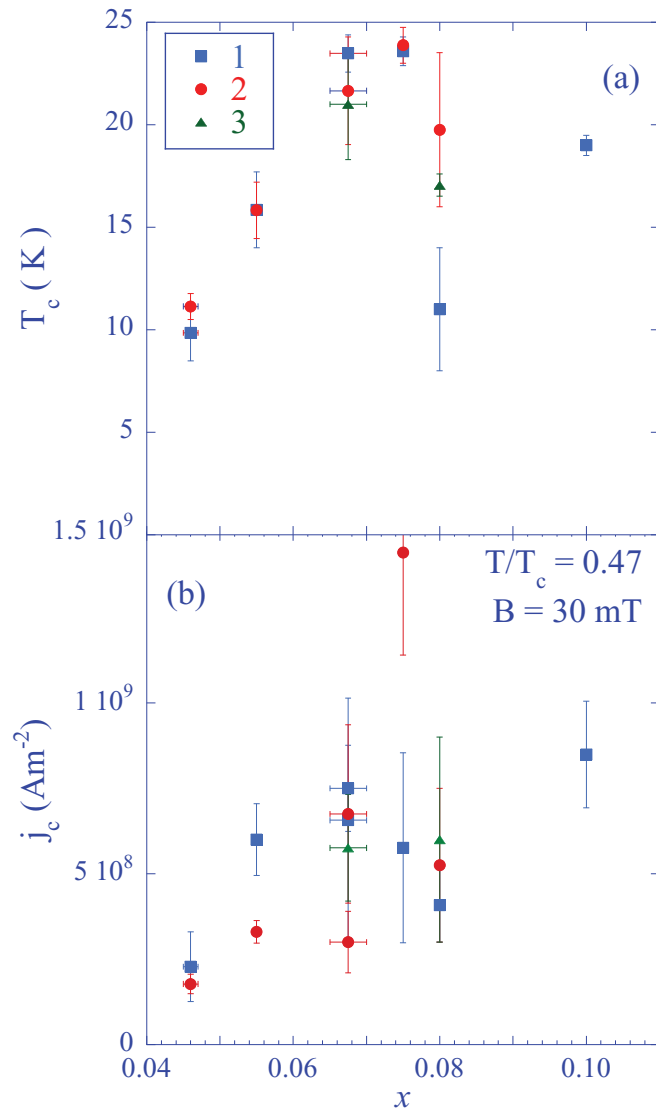
FIG. 2. (Color online) (a) Transition temperature T_c versus Co doping level. The error bars denote the local spread of T_c values within a given crystal. For each doping level, 1, 2, and 3 denote different crystals. For $x = 0.075$ and 0.1, the numbering denotes that of the decorated crystals. (b) Co doping level dependence of the critical current density j_c measured by MOI at $B = 30$ mT and a reduced temperature of $T/T_c = 0.47$.

j_c is observed. Certainly, no clear doping-dependent trend appears, as proposed in Ref. 8. The obtained critical current values are comparable to those reported in the literature for the same material.[20]

B. Vortex imaging

The Bitter decoration technique[17] was used to observe vortex structures on three of the crystals used to compile Fig. 2, more precisely, on crystal 1 of the composition with $x = 0.1$, crystal 2 with $x = 0.075$, and crystal 2 with $x = 0.055$. The decoration of crystal 2 with $x = 0.055$ was unsuccessful, presumably due to the large value of the penetration depth at low doping. The decorated patterns reveal highly disordered vortex structures as in Refs. 1,3–6. Figures 3(a) and 3(b) reveal
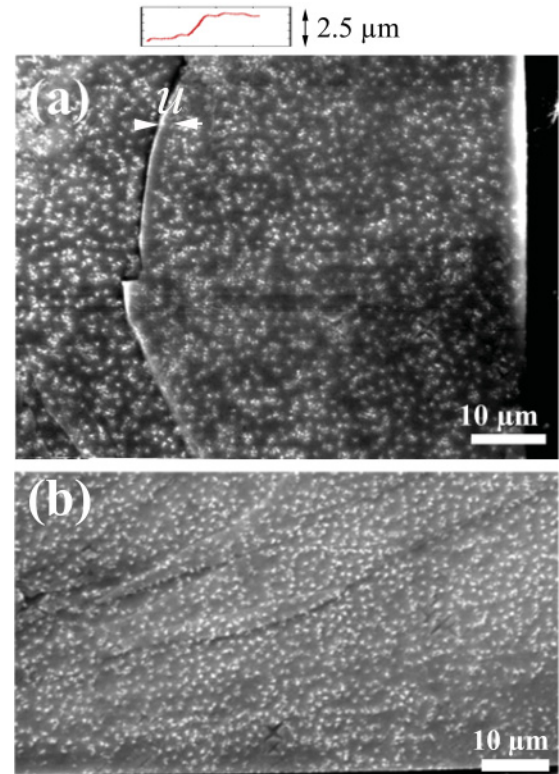

FIG. 3. Bitter decoration images of $Ba(Fe_{1-x}Co_x)_2As_2$ single crystals (a) 2.1 with $x = 0.075$ and (b) 1 with $x = 0.1$. The graph above panel (a) shows a profilometer measurement upon crossing the step that traverses the image from top to bottom; full vertical scale is 2.5 μm. The width u of the Meissner belt behind the step is also indicated in (a).

regions of high and low vortex density, as well as the formation of vortex-free zones near the crystals edges and surface steps, due to the circulating Meissner current. These images are representative of those obtained on other regions of the crystal surfaces after different cleavage runs, and on other crystals. From the images, we extract the average value of the magnetic induction as $B_{int} = n_v \Phi_0$, where n_v is the vortex density and $\Phi_0 = h/2e$ is the flux quantum. For all images we obtain an average induction $B_{int} \approx 0.8$ mT, 20% smaller than the applied field $\mu_0 H_a = 1$ mT.

Figures 4(a) and 4(b) present the Delaunay triangulations of the images in Fig. 3 for $x = 0.075$ and $x = 0.1$, respectively. Here, the blue dots represent vortices with sixfold coordination while the red dots represent vortices which have a different coordination number. The insets to Figs. 4(a) and 4(b) show the Fourier transforms of the vortex positions which once again demonstrate the absence of any order in the vortex structure.

C. Vortex configurations near surface steps

The correct determination of the distribution of vortex pinning energies in the crystal and its interpretation requires knowledge of the temperature at which the vortex ensemble was frozen in the observed configuration. To determine this, we analyze the vortex distribution near the ubiquitous steps seen on the surfaces of the crystals. Such steps result from the repeated crystal cleavage performed during the Bitter
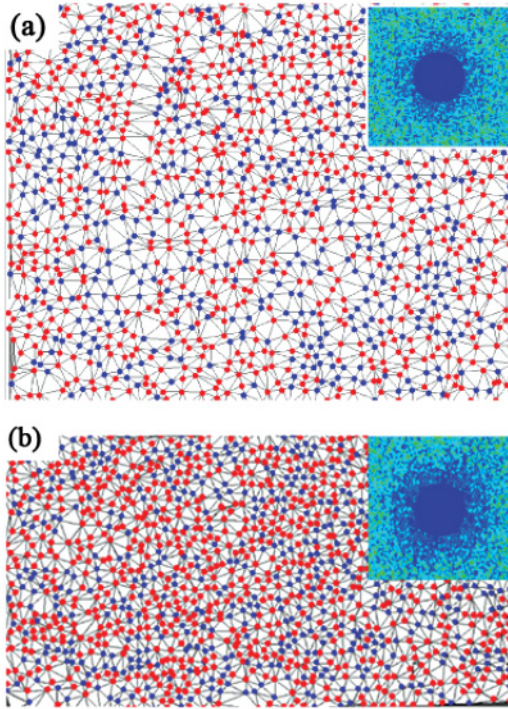
FIG. 4. (Color online) Delaunay triangulation of the vortex structure of $Ba(Fe_{1-x}Co_x)_2As_2$ single crystals (a) 2.1 with $x = 0.075$ and (b) 2 with $x = 0.1$. The blue dots represent vortices with 6 nearest neighbors while red ones represent vortices with a different coordination number. The insets show the respective Fourier transforms of the vortex positions.

decoration experiments. In zero field cooled experiments, steps act as obstacles for vortex entry into the sample; they were described in Ref. 21 as "vortex diodes."

However, the present decoration experiments are in field-cooled conditions and hence vortices nucleate in the sample at the same temperature at which the mixed state is stable. As one cools down, the Meissner screening current running along the crystal edges, but also along the surface steps, increases as the penetration depth λ_{ab} for currents running in the ab plane decreases (see Fig. 5). Thus, while cooling, vortices on the high side of the step are progressively repelled by the increasing Meissner current density $j_M \sim H_a/\lambda_{ab}$. At the same time, the proximity of the step surface results in an attractive force that can be described by an image vortex segment. Finally, the vortex lattice elasticity tends to restore a homogeneous flux
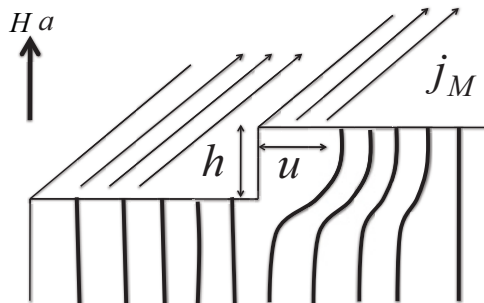

FIG. 5. Representation of vortex lines near a surface step under field-cooled conditions.

distribution near the step. The situation is therefore similar to vortex entry or exit over a surface barrier.

At the low fields of interest, the single vortex part of the tilt modulus dominates vortex elasticity,[22] so that the force balance is

$$\frac{B_{int}}{\lambda_{ab}}\left[H_a e^{-\upsilon} - \frac{B_{int}}{\mu_0}e^{-2\upsilon} - \frac{\varepsilon_\lambda^2 \varepsilon_0}{\Phi_0}\ln\left(\frac{B_{c2}}{2B_{int}}\right)\frac{u\lambda_{ab}}{h^2}\right] =$$
$$\frac{B_{int}}{\lambda_{ab}}\left[H_a e^{-\upsilon} - \frac{B_{int}}{\mu_0}e^{-2\upsilon} - \frac{\varepsilon_\lambda^2 \Phi_0 \upsilon}{4\pi\mu_0 h^2}\ln\left(\frac{B_{c2}}{2B_{int}}\right)\right] = 0.$$
(1)

Here, $\varepsilon_1 = \varepsilon_\lambda^2 \varepsilon_0$ is the vortex line tension, $\varepsilon_0 = \Phi_0^2/4\pi\mu_0\lambda_{ab}^2$ is the vortex line energy, $\varepsilon_\lambda = \lambda_{ab}/\lambda_c$ is the penetration depth anisotropy, and $\upsilon \equiv u/\lambda_{ab}$ represents the width of the vortex-free zone behind the step, u, normalized to λ_{ab}. The step running through Fig. 3(a) has a height $h = 1.5~\mu$m while the vortex-free region behind it has a width $u = 1.8~\mu$m. Estimating the penetration depth anisotropy $\varepsilon_\lambda \approx 0.16$ from Refs. 23 and 24, and with all other parameters known, Eq. (1) can be solved graphically to yield $\upsilon \sim 1.5$; that is, $\lambda_{ab} \sim 0.6u \sim 1.2~\mu$m. Combining λ_{ab} data from Refs. 6 and 23, we conclude that the observed vortex pattern is frozen at $T_f \approx 0.9T_c$.

D. Pinning energies

The intervortex interaction energy is calculated from the vortex positions obtained from the decoration images. We calculate the interaction energy

$$\mathcal{E}_{int}^i = \sum_j 2\varepsilon_0 K_0\left(\frac{|r_{ij}|}{\lambda_{ab}}\right) \tag{2}$$

per unit length along the vortices' direction. $K_0(x)$ is the lowest-order modified Bessel function, and the vortex line energy $\varepsilon_0 \propto \lambda_{ab}^{-2}$ is proportional to the superfluid density. We take into account all vortices j situated at a distance smaller than $10\lambda_{ab}$ from vortex i. This cutoff radius was chosen after verifying that the interaction energy does not change significantly if greater values of j are considered. For the determination of the energy distribution histograms, we only take into account vortices situated away from the edges of images, at a distance larger than $4\lambda_{ab}$.[25] We used in this calculation the penetration-depth value at the temperature at which the vortex structure was frozen, $\lambda_{ab}(T/T_c = 0.9)$ (see Sec. III C).

A similar procedure yields maps of the pinning force per unit length acting on an individual vortex i

$$\mathbf{f}_i = \sum_j \frac{2\varepsilon_0}{\lambda_{ab}}\frac{\mathbf{r}_{ij}}{|\mathbf{r}_{ij}|}K_1\left(\frac{|\mathbf{r}_{ij}|}{\lambda_{ab}}\right), \tag{3}$$

with $K_1(x)$ the first-order modified Bessel function. Since the system is stationary, Newton's third law requires that the repulsive force exerted by neighbor vortices be balanced by the pinning force. A map of the modulus $|\mathbf{f}_i|$ thus represents a map of the minimum pinning force acting on each vortex. In the case of a perfect lattice resulting from negligible effect of pinning, the sum (3) vanishes.
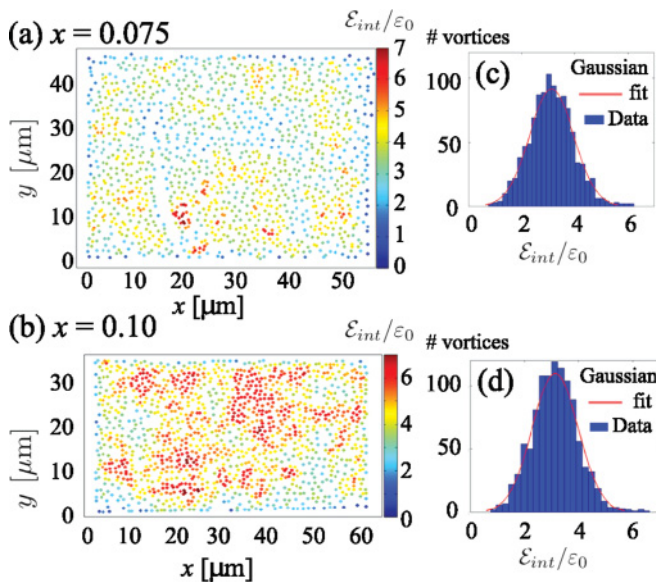
FIG. 6. (Color online) Left-hand panels: Normalized color-coded maps of the vortex interaction energy calculated from the images of Fig. 3 in Ba(Fe$_{1-x}$Co$_x$)$_2$As$_2$ single crystals with (a) $x = 0.075$ and (b) $x = 0.1$. Right-hand panels: Histograms of the normalized interaction-energy for (c) $x = 0.075$ and (d) $x = 0.1$.
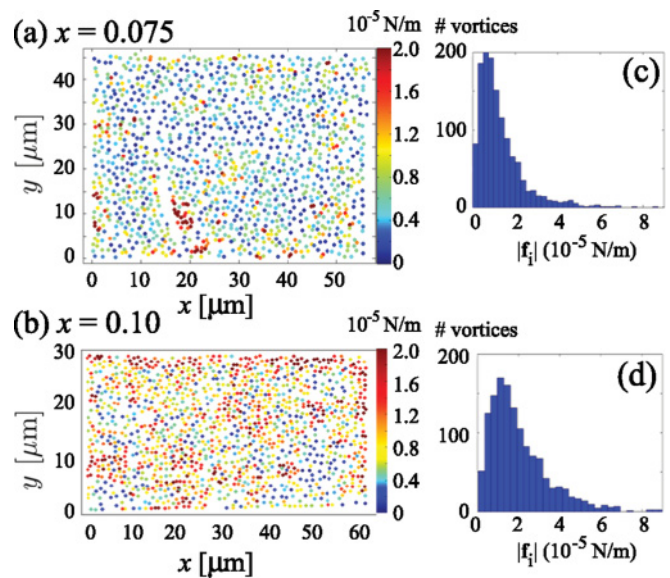

FIG. 7. (Color online) Color-coded maps of the modulus of the individual vortex pinning force per unit length, calculated from the images in Fig. 3 for Ba(Fe$_{1-x}$Co$_x$)$_2$As$_2$ single crystals with (a) $x = 0.075$ and (b) $x = 0.1$. (c) and (d) represent the pinning force distribution for $x = 0.075$ and $x = 0.1$, respectively.

We present our results by color-coded maps spanning the decoration images of Figs. 3(a) and 3(b), and by histograms of the interaction energy distribution. The interaction energy maps, with the energy-scale normalized by ε_0, are shown in Figs. 6(a) and 6(b). A granular structure of denser regions with larger interaction energy, and dilute regions with smaller $\mathcal{E}_{int}$, is clearly visible. This granularity is translated into broad vortex interaction-energy histograms as shown in Figs. 6(c) and 6(d). The histograms are reasonably well fitted by a Gaussian distribution. The standard deviations of these histograms are of the order of 23%, in contrast with 50% for the rather regular vortex structures[26] of the same density imaged in the high-T_c material Bi$_2$Sr$_2$CaCu$_2$O$_{8+\delta}$. However, as a result of the high reduced temperature T_f/T_c at which the vortex ensemble is frozen, the mean interaction energy (normalized by ε_0) is ten times larger in Ba(Fe$_{1-x}$Co$_x$)$_2$As$_2$ than in Bi$_2$Sr$_2$CaCu$_2$O$_{8+\delta}$.[27]

The reduced temperature T_f/T_c at which the vortex ensemble is frozen not only affects the deduced interaction energies, but also has a profound effect on the (orientational) order observed in the decorated vortex ensemble.[28] Pardo *et al.* reported[28] that in optimally doped Tl$_2$Ba$_2$CuO$_{6-\delta}$ with a broad magnetically reversible phase, and concomitantly low T_f/T_c, Bitter decoration yields a regular triangular lattice, while decorated vortex ensembles in the overdoped material with a narrow reversible temperature range (and high T_f/T_c) are amorphous. At the origin of this effect is the high mobility of vortices just above T_f in materials with a wide reversible regime, such as Bi$_2$Sr$_2$CaCu$_2$O$_{8+\delta}$ or optimally doped Tl$_2$Ba$_2$CuO$_{6-\delta}$. On the other hand, the low mobility of the vortices just above T_f due to strong pinning in the vortex liquid phase in materials [such as, apparently, Ba(Fe$_{1-x}$Co$_x$)$_2$As$_2$] that have a narrow reversible regime yields an amorphous vortex ensemble.

Figure 7 shows maps of the modulus of the pinning force of individual vortices per unit length of the vortex lines. The pinning energy shows some correlation with the interaction energy at the local scale: Regions of large (small) $\mathcal{E}_{int}$ generally correspond to regions of large (small) $|\mathbf{f}_i|$. There is noticeable inhomogeneity on scales smaller than the apparent grain size. The juxtaposition of a region with homogeneous large superfluid density (i.e., ε_0) with a region of homogeneous small ε_0 would give rise to a larger pinning force at the interface only. In the images, fluctuations of the pinning force within grains of similar $\mathcal{E}_{int}$ are observable. Therefore, inhomogeneity of the superconducting parameters exists not only on the μm scale of the images, but also on smaller length scales.

It is interesting to note that the rendered pinning forces are simply related to a metastable current density $\mathbf{j}_i$, *running through each vortex*, as $\mathbf{f}_i = (\Phi_0/|\mathbf{B}|)\mathbf{B} \times \mathbf{j}_i$. The average pinning force per unit length of 5×10^{-6} N/m, with local maxima of up to 6×10^{-5} N/m, implies local currents of the order of 2.5×10^9 A m^{-2}. Maximum currents are of the order of 3×10^{10} A m^{-2}, comparable to the low-temperature value of the critical current density.

IV. DISCUSSION

Since the vortex locations result from the balance between intervortex repulsion and the interaction $\mathcal{E}_p$ of individual vortices with the pinning impurities, one has, at T_f, $\mathcal{E}_{int} = \mathcal{E}_p$. The position of the maximum and the width of the interaction-energy distributions [see Fig. 6(c) and 6(d)] are therefore determined by, respectively, the mean and the standard deviation of the pinning energies, at T_f, of the individual vortices in a given image. In particular, the displacement of the maximum of the distribution with respect to the position of the δ-peak

energy distribution of a perfect vortex lattice of the same density is a measure of the mean pinning energy. As far as the vortex densities of Fig. 6 are concerned, the average $B_{int} = 0.8$ mT yields a δ-peak maximum at $\mathcal{E}_{int} = 2.5\varepsilon_0$. By comparison, the maxima of the distributions for both investigated crystals in Figs. 6(a) and 6(b) occur at $\mathcal{E}_{int} \approx 3.2\varepsilon_0$. The average pinning energy per unit length is therefore $\mathcal{E}_p \sim 0.7\varepsilon_0$, while the variance in pinning energy is given by the width of the distribution, $(\langle \mathcal{E}_p^2 \rangle - \langle \mathcal{E}_p \rangle^2)^{1/2} \sim 0.5\varepsilon_0$. Note that $3.2\varepsilon_0$ corresponds to the interaction energy of a triangular vortex lattice with $\Phi_0 n_v = 1$ mT, i.e., the external field applied during the experiments. This means that the average interaction energy is determined by vortex-rich areas, with $\Phi_0 n_v \gtrsim 1$ mT. However, the vortex density also presents vortex-poor areas so that the average $B_{int} = 0.8$ mT.

The large absolute values of the inferred pinning energies can be understood if one combines the notion that the crystals show local variations both of the critical temperature $T_c = T_c(\mathbf{r})$ and of the line energy $\varepsilon_0 = \varepsilon_0(\mathbf{r}, T)$, and that $T_f / T_c \lesssim 1$. As the crystal is cooled below T_c, vortices will avoid regions of higher T_c and ε_0, and accumulate in regions with lower values of these parameters. They will remain trapped in such regions as the temperature is lowered below T_f. The large absolute values and variances of the pinning energies revealed by the decoration experiment are caused by the local variations of $T_c(\mathbf{r})$, which manifest themselves through the temperature dependence of the line energy, $\varepsilon_0(\mathbf{r}, T) = \varepsilon_0(\mathbf{r}, 0)[1 - T/T_c(\mathbf{r})]$. More specifically, the width of the inferred pinning-energy distribution (Fig. 6) should correspond to the width $\Delta\varepsilon_0(T_f)$ of the line-energy distribution,

$$0.5\varepsilon_0(0)(1 - T_f/T_c) \sim \Delta\varepsilon_0(T_f). \qquad (4)$$

Near to the critical temperature, $\Delta\varepsilon_0(T) = \varepsilon_0(0)T\Delta T_c/T_c^2$ is determined mainly by the width ΔT_c of the distribution of local $T_c(\mathbf{r})$. Solving Eq. (4) then yields $T_f = T_c/[1 + \Delta T_c/0.5T_c]$. Taking $T_c = 24$ K, and estimating $\Delta T_c \approx 0.8$ K from the DMO data of Fig. 1, one obtains a freezing temperature $T_f = 0.94T_c$ for $x = 0.075$; the same exercise with $T_c = 19$ K and $\delta T_c = 0.5$ K yields and $T_f = 0.95T_c$ for the crystal with $x = 0.1$. Thus, the analysis of the inhomogeneous and disordered vortex distribution, as well as the vortex distribution near steps and edges, is fully consistent with the observed patterns having been frozen between $T = 0.9T_c$ and $0.95T_c$. We can draw the same conclusion from the local variations of the vortex density. For example, for crystal 2 with $x = 0.075$, the largest local vortex gradient corresponds to 0.15 mT/μm or 1×10^8 A m^{-2}. This value is consistent with the critical current density of Ba(Fe$_{0.925}$Co$_{0.075}$)$_2$As$_2$ crystal 2 at 23 K.

At low temperatures, the spatial variations of the magnitude of the line energy $\varepsilon_0(\mathbf{r}, 0)$ are dominant. These correspond to the variations in space of the superfluid density[5] and are responsible for the nonzero low-T pinning force arising from spatial inhomogeneity. A spatially homogeneous superfluid density would imply a vanishing (or logarithmically weak) pinning energy at low T, at odds with the existence of a large critical current density (see, e.g., Fig. 8). As in all charge-doped single-crystalline iron-based superconductors, the critical current of Ba(Fe$_{1-x}$Co$_x$)$_2$As$_2$ is composed of a contribution from strong, extrinsic pins, and from a contribution from pinning by atomic sized point pins. The latter dominates at high fields
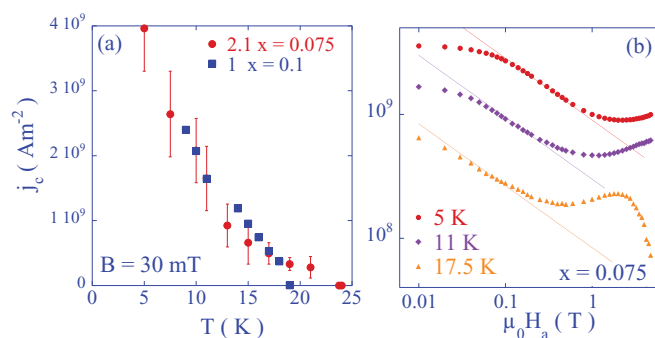

FIG. 8. (Color online) Critical-current densities in our Ba(Fe$_{0.925}$Co$_{0.075}$)$_2$As$_2$ crystals. (a) Temperature dependence of the low-field j_c of crystals 1 ($x = 0.1$) and 2.1 ($x = 0.075$), as obtained from MOI. Error bars represent the dispersion of j_c within a given crystal. (b) Field dependence of j_c for crystal 2.1, obtained from magnetic hysteresis measurements using a SQUID magnetometer. Straight lines indicate fits with Eq. (6); see Sec. IV.

[here, above 1 T at 5 K, and above 0.2 T at 17.5 K; see Fig. 8(b)],[29] while the former contribution manifests itself as a low-field plateau,[16,30]

$$j_c = \pi^{1/2} \frac{f_p}{\Phi_0 \varepsilon_\lambda} \left(\frac{U_p n_i}{\bar{\varepsilon}_0} \right)^{1/2} \qquad (B \ll B^*), \qquad (5)$$

followed by a power law in the flux density B,[16,30]

$$j_c(B) = \frac{f_p}{\Phi_0 \varepsilon_\lambda} \left(\frac{U_p n_i}{\varepsilon_0} \right) \left(\frac{\Phi_0}{B} \right)^{1/2} \qquad (B \gg B^*). \qquad (6)$$

The crossover field B^* is that above which the number of effective pins per vortex is limited by the intervortex repulsion, f_p is the maximum pinning force exerted by a single strong pin, n_i is the pin density, and $U_p/[J]$ is the pinning energy gained by a vortex line traversing such a pin. The measurement of the low-field critical current density $j_c(0)$ and the slope $\partial j_c(B)/\partial B^{-1/2}$ allows one to eliminate n_i and to obtain $f_p = \pi \Phi_0^{3/2} \varepsilon_\lambda \{j_c^2(0)/[\partial j_c(B)/\partial B^{-1/2}]\}$ from experimental data without further assumptions. We find that, at 5 K, $f_p \approx 3 \times 10^{-13}$ N for both Ba(Fe$_{0.925}$Co$_{0.075}$)$_2$As$_2$ crystal 2.1 and Ba(Fe$_{0.9}$Co$_{0.1}$)$_2$As$_2$ crystal 1.

The identification of the strong pins with regions of lower $\varepsilon_0(T)$ means that f_p should be interpreted in terms of the local maxima of the position-dependent force $f(\mathbf{r}) = \int_{\delta z} \nabla \varepsilon_0(\mathbf{r}) dz$ experienced by vortices as they move through the sample. Here δz is the maximum extent of a region of low $\varepsilon_0(T)$ along the field direction. We approximate

$$f_p \sim \Delta\varepsilon_0 \left(\frac{\delta z}{\delta \varrho} \right), \qquad (7)$$

where $\delta \varrho$ is the length scale characterizing the disorder in the direction perpendicular to the field, and $\Delta\varepsilon_0$ is the standard deviation of the $\varepsilon_0(\mathbf{r})$ distribution in the crystal. The pinning energy $U_p \sim f_p \delta \varrho$. A comparison of Eq. (7) with the value of f_p obtained from j_c yields $\Delta\varepsilon_0 \sim 3 \times 10^{-13}$ J m^{-1} for a unit aspect ratio $\delta z/\delta \varrho$.

In a next step, we evaluate the ratio of $f_p/|\bar{\mathbf{f}}_i|$ to obtain the average distance between effective pins, $\bar{\mathcal{L}} = 60$ nm. Using Eq. (17) of Ref. 30, which has $\bar{\mathcal{L}} = (\varepsilon_1/\pi n_i U_p)^{1/2}$,

one finds $(n_i \delta z)^{-1/2} \sim 60$ nm. With all parameters known, the low-field value of the critical current density is reproduced as

$$j_c \approx \pi^{1/2} \frac{\Delta\varepsilon_0}{\Phi_0 \varepsilon_\lambda} \sqrt{n_i \delta z} \frac{\delta z}{\delta \varrho} \sqrt{\frac{\Delta\varepsilon_0}{\bar{\varepsilon}_0}} = 8 \times 10^9 \text{ A m}^{-2}, \quad (8)$$

in fair agreement with the data of Fig. 8(a). The investigated features of vortex pinning in Ba(Fe$_{1-x}$Co$_x$)$_2$As$_2$, including the disordered vortex patterns and the critical current density, are therefore consistently described by the presence of spatial variations of the superfluid density on the scale of *several dozen* nanometers, in agreement with the conjecture of Ref. 9.

Note that the observed spatial structures at the macroscopic (Fig. 1) and mesoscopic (Fig. 3) levels are not those responsible for the critical current. The random vortex positions observed in the decoration experiments are determined by the underlying nanoscale disorder, an observation consistent with the fact that disordered vortex structures have been observed up to high fields.[1,3]

One may speculate about the possible link between the existence of nm-sized regions of reduced superfluid density, the local variation of the dopant atom density, and the effect of the overall doping level. For instance, one would expect the fluctuations of the Co density to be more important at lower doping levels, yielding larger local fluctuations of ε_0. However, given the much larger values of the penetration depth at low doping, we have not been successful in performing Bitter decorations on the relevant crystals. Recent STS studies have reported substantial variations of the value of the superconducting gap on a scale of 10 to 20 nm.[7,11] These local variations of the gap magnitude should correspond to the variations of the critical temperature and therefore lead to vortex pinning. Although it is tempting to relate our results to the nanoscale disorder observed in the STS gap maps, it should be remarked that the spatial scale of the variations in the gap maps is a factor of 3–6 smaller than that found from the analysis of the data presented here. This would

correspond to a concomitantly larger j_c in the samples used in Refs. 7,11.

V. CONCLUSION

Bitter-decoration imaging of the disordered vortex distribution in superconducting Ba(Fe$_{1-x}$Co$_x$)$_2$As$_2$ single crystals with $x = 0.075$ and $x = 0.1$ reveals a substantial local variation of pinning energies and pinning forces. The magnitude of these fluctuations is suggested to stem from nanoscale spatial variations of T_c and/or the superfluid density due to an inhomogeneous distribution of dopant atoms. The spatial scale of the variations is inferred from the correlation of the features of the vortex distributions with global and local critical current density measurements. The macroscopic spatial variations of the critical temperature observed using magneto-optical imaging give an idea of the magnitude of the T_c variations in the crystals, but are unrelated to the measured pinning properties. The same can be said for mesoscopic disorder structures observed by single-vortex imaging. An important corollary of our work is the fact that the observed vortex distributions are frozen, at a length scale of the lattice spacing, at a high temperature close to T_c.

[1]M. R. Eskildsen, L. Ya. Vinnikov, I. S. Veshchunov, T. M. Artemova, T. D. Blasius, J. M. Densmore, C. D. Dewhurst, N. Ni, A. Kreyssig, S. L. Bud'ko, P. C. Canfield, and A. I. Goldman, Physica C **469**, 529 (2009).

[2]M. R. Eskildsen, L. Ya. Vinnikov, T. D. Blasius, I. S. Veshchunov, T. M. Artemova, J. M. Densmore, C. D. Dewhurst, N. Ni, A. Kreyssig, S. L. Bud'ko, P. C. Canfield, and A. I. Goldman, Phys. Rev. B **79**, 100501 (2009).

[3]D. S. Inosov, T. Shapoval, V. Neu, U. Wolff, J. S. White, S. Haindl, J. T. Park, D. L. Sun, C. T. Lin, E. M. Forgan, M. S. Viazovska, J. H. Kim, M. Laver, K. Nenkov, O. Khvostikova, S. Kuhnemann, and V. Hinkov, Phys. Rev. B **81**, 014513 (2010).

[4]L. Ya. Vinnikov, T. M. Artemov, I. S. Veshchunov, N. D. Zhigadlo, J. Karpinski, P. Popovich, D. L. Sund, C. T. Lind, and A. V. Boris, JETP Lett. **90**, 299 (2009).

[5]B. Kalisky, J. R. Kirtley, J. G. Analytis, J. H. Chu, I. R. Fisher, and K. A. Moler, Phys. Rev. B **83**, 064511 (2011).

[6]L. Luan, O. M. Auslaender, T. M. Lippman, C. W. Hicks, B. Kalisky, J.-H. Chu, J. G. Analytis, I. R. Fisher, J. R. Kirtley, and K. A. Moler, Phys. Rev. B **81**, 100501(R) (2010).

[7]Yi Yin, M. Zech, T. L. Williams, and J. E. Hoffman, Physica C **469**, 535 (2009).

[8]R. Prozorov, M. A. Tanatar, N. Ni, A. Kreyssig, S. Nandi, S. L. Bud'ko, A. I. Goldman, and P. C. Canfield, Phys. Rev. B **80**, 174517 (2009).

[9]A. Yamamoto, J. Jaroszynski, C. Tarantini, L. Balicas, J. Jiang, A. Gurevich, D. C. Larbalestier, R. Jin, A. S. Sefat, M. A. McGuire, B. C. Sales, D. K. Christen, and D. Mandrus, Appl. Phys. Lett. **94**, 062511 (2009).

[10]Y. Yin, M. Zech, T. L. Williams, X. F. Wang, G. Wu, X. H. Chen, and J. E. Hoffman, Phys. Rev. Lett. **102**, 097002 (2009).

[11]F. Massee, Y. Huang, R. Huisman, S. de Jong, J. B. Goedkoop, and M. S. Golden, Phys. Rev. B **79**, 220517 (2009).

[12]Y. Fasano, I. Maggio-Aprile, N. D. Zhigadlo, S. Katrych, J. Karpinski, and O. Fischer, Phys. Rev. Lett. **105**, 167005 (2010).

[13] F. Rullier-Albenque, D. Colson, A. Forget, and H. Alloul, Phys. Rev. Lett. **103**, 057001 (2009).

[14] E. H. Brandt, Phys. Rev. B **58**, 6506 (1998).

[15] L. A. Dorosinskii, M. V. Indenbom, V. I. Nikitenko, Yu.A. Ossip'yan, A. A. Polyanskii, and V. K. Vlasko-Vlasov, Physica C **203**, 149 (1992).

[16] C. J. van der Beek, G. Rizza, M. Konczykowski, P. Fertey, I. Monnet, T. Klein, R. Okazaki, M. Ishikado, H. Kito, A. Iyo, H. Eisaki, S. Shamoto, M. E. Tillman, S. L. Bud'ko, P. C. Canfield, T. Shibauchi, and Y. Matsuda, Phys. Rev. B **81**, 174517 (2010).

[17] Y. Fasano and M. Menghini, Supercond. Sci. Technol. **21**, 023001 (2008).

[18] C. P. Bean, Phys. Rev. Lett. **8**, 6 (1962).

[19] E. Zeldov, J. R. Clem, M. McElfresh, and M. Darwin, Phys. Rev. B **49**, 9802 (1994).

[20] R. Prozorov, N. Ni, M. A. Tanatar, V. G. Kogan, R. T. Gordon, C. Martin, E. C. Blomberg, P. Prommapan, J. Q. Yan, S. L. Bud'ko, and P. C. Canfield, Phys. Rev. B **78**, 224506 (2008).

[21] F. Pardo, F. de la Cruz, P. L. Gammel, E. Bucher, C. Ogelsby, and D. J. Bishop, Phys. Rev. Lett. **79**, 1369 (1997).

[22] A. Sudbø and E. H. Brandt, Phys. Rev. Lett. **66**, 1781 (1991).

[23] R. Prozorov, M. A. Tanatar, R. T. Gordon, C. Martin, H. Kim, V. G. Kogan, N. Ni, M. E. Tillman, S. L. Bud'ko, and P. C. Canfield, Physica C **469**, 582 (2009).

[24] J. Haenisch, K. Iida, S. Haindl, F. Kurth, A. Kaufmann, M. Kidszun, T. Thersleff, J. Freudenberger, L. Schultz, and B. Holzapfel, IEEE Transactions on Applied Superconductivity **21**, 2887 (2011).

[25] We have checked our summing method by calculating the interaction energy distribution of a perfect Abrikosov lattice, which should be a δ function. After neglecting the contribution from the vortices situated less than $4\lambda_{ab}$ from the edges of the image, we obtain, for the perfect lattice, a well-defined δ peak for the interaction energy distribution.

[26] Y. Fasano, M. De Seta, M. Menghini, H. Pastoriza, and F. de la Cruz, Proc. Natl. Acad. Sci. USA **102**, 3898 (2005).

[27] The calculated distributions depend quite sensitively on the value of λ_{ab}, and, by implication, on the temperature at which the vortex ensemble was frozen. A larger λ_{ab} yields a much larger energy scale as well as more symmetric distributions. Analyzing data on $Bi_2Sr_2CaCu_2O_8$ and $Ba(Fe_{1-x}Co_x)_2As_2$ using the same (low temperature) value $\lambda_{ab} = 300$ nm (Ref. [6]) yields distributions that are three times broader for $Ba(Fe_{1-x}Co_x)_2As_2$, but with a mean value that is only 10% larger.

[28] F. Pardo, A. P. Mackenzie, F. de la Cruz, and J. Guimpel, Phys. Rev. B **55**, 14610 (1997).

[29] C. J. van der Beek, M. Konczykowski, S. Kasahara, T. Terashima, R. Okazaki, T. Shibauchi, and Y. Matsuda, Phys. Rev. Lett. **105**, 267002 (2010).

[30] C. J. van der Beek, M. Konczykowski, A. Abaloshev, I. Abal'osheva, P. Gierlowski, S. J. Lewandowski, M. V. Indenbom, and S. Barbanera, Phys. Rev. B **66**, 024523 (2002).